

RESEARCH ARTICLE

10.1002/2014JA020860

Key Points:

- Auroral sounding rocket observations are reported
- We combine ground-based, in situ, and modeling results
- We report gradient scale lengths in auroral structures

Correspondence to:

K. A. Lynch,
kal@dartmouth.edu

Citation:

Lynch, K. A., et al. (2015), MICA sounding rocket observations of conductivity-gradient-generated auroral ionospheric responses: Small-scale structure with large-scale drivers, *J. Geophys. Res. Space Physics*, 120, 9661–9682, doi:10.1002/2014JA020860.

Received 20 NOV 2014

Accepted 2 OCT 2015

Accepted article online 5 OCT 2015

Published online 3 NOV 2015

MICA sounding rocket observations of conductivity-gradient-generated auroral ionospheric responses: Small-scale structure with large-scale drivers

K. A. Lynch¹, D. L. Hampton², M. Zettergren³, T. A. Bekkeng⁴, M. Conde², P. A. Fernandes¹, P. Horak¹, M. Lessard⁵, R. Miceli⁶, R. Michell^{7,8}, J. Moen⁴, M. Nicolls⁹, S. P. Powell⁶, and M. Samara⁷

¹Department of Physics and Astronomy, Dartmouth College, Hanover, New Hampshire, USA, ²Geophysical Institute, University of Alaska Fairbanks, Fairbanks, Alaska, USA, ³Department of Engineering, Embry-Riddle Aeronautical University, Daytona Beach, Florida, USA, ⁴Department of Physics, University of Oslo, Oslo, Norway, ⁵Space Science Center, University of New Hampshire, Durham, New Hampshire, USA, ⁶School of Electrical & Computer Engineering, Cornell University, Ithaca, New York, USA, ⁷NASA Goddard Space Flight Center, Greenbelt, Maryland, USA, ⁸Department of Astronomy, University of Maryland, College Park, Maryland, USA, ⁹SRI International, Menlo Park, California, USA

Abstract A detailed, in situ study of field-aligned current (FAC) structure in a transient, substorm expansion phase auroral arc is conducted using electric field, magnetometer, and electron density measurements from the Magnetosphere-Ionosphere Coupling in the Alfvén Resonator (MICA) sounding rocket, launched from Poker Flat, AK. These data are supplemented with larger-scale, contextual measurements from a heterogeneous collection of ground-based instruments including the Poker Flat incoherent scatter radar and nearby scanning doppler imagers and filtered all-sky cameras. An electrostatic ionospheric modeling case study of this event is also constructed by using available data (neutral winds, electron precipitation, and electric fields) to constrain model initial and boundary conditions. MICA magnetometer data are converted into FAC measurements using a sheet current approximation and show an up-down current pair, with small-scale current density and Poynting flux structures in the downward current channel. Model results are able to roughly recreate only the large-scale features of the field-aligned currents, suggesting that observed small-scale structures may be due to ionospheric feedback processes not encapsulated by the electrostatic model. The model is also used to assess the contributions of various processes to total FAC and suggests that both conductance gradients and neutral dynamos may contribute significantly to FACs in a narrow region where the current transitions from upward to downward. Comparison of Poker Flat Incoherent Scatter Radar versus in situ electric field estimates illustrates the high sensitivity of FAC estimates to measurement resolution.

1. Introduction

Auroral activity modifies the ionosphere by both depositing and extracting energy and particles. When auroral precipitation is structured in space, the resulting ionospheric structuring can become a source of free energy and currents. The details leading to ionospheric feedback mechanism [Russell *et al.*, 2013] and the ionospheric Alfvén resonator (IAR) [Lysak and Song, 2011] have a long theoretical heritage beginning with the effects of simple homogeneous precipitation [Reiff, 1984] and advancing through various levels of complexity [Mallinckrodt and Carlson, 1978; Lysak, 1991; Streltsov and Lotko, 2008; Zettergren *et al.*, 2010; Russell *et al.*, 2010]. Quantitative observational confirmations of these reasonable theories, however, are few and far between, because of the difficulties inherent in measuring spatial structuring in situ. Various specific examples exist [Doe *et al.*, 1993; Lanchester *et al.*, 1996, 1998; Marklund *et al.*, 2001; Karlsson *et al.*, 2007; Semeter *et al.*, 2009; Semeter and Doe, 2002] each addressing one part of the question. Recent measurements from the Advanced Modular Incoherent Scatter Radar systems have begun to add to these observations, most recently for cases involving polar cap patches, through volumetric measurements of ionospheric state parameters [Dahlgren *et al.*, 2012].

It would be useful to be able to calculate, given auroral imaging histories, both the magnetospheric energy and particle input to the ionosphere, and the ionospheric response. The large-scale structuring of these processes can be found by inverting the imagery. There are small-scale response signatures, however,

which are not captured by imagery or remote sensing, and which need to be modeled for a complete ionospheric coupling scenario to be calculated. Interesting unknowns include the significance of these small-scale responses in the aggregate, as well as the gradient scale lengths and hysteresis effects underlying these responses. (Here we use a definition of the characteristic scale length of a gradient of a scalar field f as $L_{\nabla}(f) = f_{\text{avg}}/|\nabla f|$.) Once these can be quantified, understood, and modeled, then the large-scale remote observations can be used to drive models of these unobserved, but perhaps significant, ionospheric coupling processes.

In this manuscript, we present a detailed observational case study of a particular nightside auroral event which allows a direct comparison of in-situ-observed small-scale structures and remote sensing on larger scales. The observations include in situ particle and field measurements from a 325 km apogee sounding rocket mission, an array of ground-based imagers, the Poker Flat Incoherent Scatter Radar (PFISR), and the Scanning Doppler Imager (SDI) neutral wind measurement array. With this assemblage of data we can examine an example case study of nightside auroral arcs behind a westward traveling surge. We can use the observations to drive an electrostatic and chemistry model of the auroral ionosphere and examine which features of the observations are captured by the model. In particular, we examine small-scale downward currents at the edge and poleward of a localized active arc. We present this event as an example of an ionospheric feedback mechanism, in which conductivity gradients in the lower ionosphere, coupled with perpendicular-to- \mathbf{B} electric fields, become sources of field-aligned currents which contribute to the magnetosphere-ionosphere current system, a process not necessarily involving a resonant feedback instability, as described in *Russell et al.* [2013].

Other studies of in situ field-aligned current observations include the extensive FAST observations of both precipitating and upgoing electrons [*Paschmann*, 2002], showing the common occurrence of sheet-like current systems and the extent to which observable energetic electrons carry those currents; other studies showed that not all auroral current systems are sheetlike [*Hwang et al.*, 2006a, 2006b]. More recent, and lower altitude, studies include *Kaeppler* [2013], for the ACES sounding rocket, which also looked at closure currents and ionospheric conductivity.

Here for the Magnetosphere-Ionosphere Coupling in the Alfvén Resonator (MICA) rocket event, we focus on arc edge effects and outline the electrodynamic versus electrostatic nature of the currents; also, we attempt to account for thermospheric winds. For our event study we combine the observational context generated from inverted ground-based array data, the in situ measurements along the sounding rocket trajectory, and the simulated responses, so that we can validate the modeled response to one specific example driver. Determining which spatial scales of forcing cause observable differences in ionospheric parameters is critical for merging magnetospheric and ionospheric models for coupling studies.

The next section (section 2) describes the terms of the current continuity equation and the basic underlying ionospheric feedback processes relevant to auroral coupling. Section 3.1 describes the instrumentation and section 3.2 introduces the observations of the event. Figures 1 and 2 in this section provide an overview of the event we wish to study, from first, a large-scale view of the arc systems and then focusing in to a finer-scale view of features at the edge of one particular auroral feature. In Figure 3 we illustrate the connection between the in situ observations of the magnetic field deflections and the structure of the associated visible arc. Next, section 4 discusses the interpretation of these observations in the context of the terms of the current continuity equation. Figure 4 shows the calculation of field-aligned current from the curl of the magnetometer data, a quantification of the comparison shown in Figure 3. Figure 5 shows the relationship between the DC electric field data and the visible structures; paralleling Figure 3 which illustrates the $\nabla \times \mathbf{B}$ signatures, this figure illustrates the $\nabla \cdot \mathbf{E}$ signatures. Then, Figures 6 and 7 compare the $\nabla \times \mathbf{B}$ and $\nabla \cdot \mathbf{E}$ signatures to each other, first, on large scales and then on finer scales, in the context of the current continuity equation. In section 5, we draw comparisons between these observations and an electrostatic ionospheric chemistry model. Section 6 discusses the implications and draws conclusions. Appendix A provides a different view of the same event, from the larger-scale Poker Flat Incoherent Scatter Radar (PFISR) facility. Associated studies of the same event include *Zettergren et al.* [2014], a model study of large-scale density cavities driven by inputs from the ground-based data, and Hampton et al. (in preparation, 2015), a description of the capabilities and limitations of the ground-based data inversion process.

2. Background

The magnetosphere and ionosphere are coupled by the currents, Poynting flux, and plasma that flow between them [Moore and Horwitz, 2007]. Simplistic models of the ionosphere include it in the system as a uniform passive slab at the foot point of the connecting flux tubes. Increasingly realistic models allow for altitude structuring of the ionosphere, with different bulk parameters at different altitudes [Lysak, 1999], and for varying temporal responses, with different transmissions and reflections of Poynting flux for different frequencies [Lysak, 1985; Knudsen et al., 1990]. Different types of auroral activity span a large range of possible spatial scales for structured nightside auroral input [Paschmann, 2002; Newell et al., 2009]. Separately, quasi-static arcs such as early evening quiet arcs versus Alfvénic structures at the poleward boundary have very different (hard and soft) precipitating electron energy spectra, radically changing their interactions with the ionospheric background [Lynch et al., 2007] because of the altitude of energy deposition for each of these populations. Transport models such as TRANSCAR [Lilensten and Blelly, 2002; Blelly et al., 2005], a one-dimensional time-dependent model of the ionosphere with both fluid and kinetic models, show completely different ionospheric responses to forcing from different spectral shapes of precipitating electron distribution functions.

However, another important component of the ionospheric role in magnetosphere-ionosphere (M-I) coupling derives from the perpendicular structuring of the ionosphere. Horizontal structuring of perpendicular-to- \mathbf{B} ionospheric electric fields and conductivity makes the ionosphere a source of field-aligned currents, an idea which is an essential building block of magnetosphere-ionosphere coupling. Under a steady state formulation, the total field-aligned current can be viewed as being composed of contributions from this horizontal structuring, such that from current continuity, in the electrostatic limit, the parallel current density may be written [Paschmann, 2002; Brekke, 1997; Kaeppler, 2013]:

$$J_{\parallel} = \Sigma_p(\nabla_{\perp} \cdot \mathbf{E}_{\perp}) + \nabla_{\perp} \Sigma_p \cdot \mathbf{E}_{\perp} - \nabla_{\perp} \Sigma_h \cdot (\hat{\mathbf{e}}_1 \times \mathbf{E}_{\perp}) \quad (1)$$

where \mathbf{e}_1 is a unit vector along the geomagnetic field, Σ_p and Σ_h are the conductances from the height-integrated Pedersen and Hall conductivities, and \mathbf{E}_{\perp} is the perpendicular electric field. Ionospheric conductance gradients in the presence of background convection have been shown to be a significant source of field-aligned currents [St.-Maurice et al., 1996; Noël et al., 2000; de Boer et al., 2010]. Furthermore, since field-aligned currents change the ionospheric conductivity, allowing for gradients in the conductivity and for inductive effects creates an interesting ionospheric feedback mechanism [Russell et al., 2010, 2013] and can also result in instability [Streltsov and Lotko, 2008] and phase mixing [Lysak and Song, 2011]. For even moderate values of conductivity and scale size, these gradient-generated field-aligned currents are significant (of the order $5 \mu\text{A}/\text{m}^2$ [Kelley, 1989]), and for finer structures the results are comparably larger [de Boer et al., 2010]. Thus, quantifying these gradients is significant for our understanding of M-I coupling in both a steady state regime and in situations where inductive interactions dominate.

Discussions of this ionospheric feedback effect from current continuity have extensive literature, from early studies of DC coupling and empirical measures of Σ_p from precipitation [Reiff, 1984] to modern simulations of Alfvénic coupling [Streltsov and Lotko, 2008; Cohen et al., 2013]. Magnetospheric observations of ionospheric control of coupling processes include the Cluster study of the broadening of an auroral downward current region [Marklund et al., 2001]. Ionospheric observations include the broadening of visible signatures interpreted as return current regions [Michell et al., 2008]. Thus, we know, both theoretically and observationally, that this ionospheric structure matters to our understanding of coupling. Still, there are almost no observations of the gradient scale lengths of this structuring. Even the PFISR radar has a beam width of several kilometers and a horizontal integration pixel of $\sim 100 \text{ km}^2$ at a range of 200 km, and a beam-to-beam spacing of many tens of kilometers in the F region (for our 15-beam pattern). Radars generally cannot probe the kilometer-scale gradient scale lengths of arc edge effects that are indicated by imaging and by in-situ-observed arc boundaries. Our goal here is to quantify these scales for one case study and to see the extent to which an ionospheric simulation, such as that of Zettergren and Semeter [2012], can accurately represent the effects of structuring on different scales. This exercise will yield critical insight into the minimum scale sizes necessary for capturing effects that are significant for M-I coupling.

3. Observations

3.1. Instrumentation

The MICA (Magnetosphere-Ionosphere Coupling in the Alfvén Resonator) sounding rocket mission (NASA 36.273) was launched from the Poker Flat Research Range in central Alaska on 19 February 2012 at 054106.745UT. It reached an apogee of 325.4 km 297.5s after launch. The science payload split into a main payload and a subpayload. The Cornell University subpayload carried the electric field instrumentation [Lundberg *et al.*, 2012a, 2012b]. The main payload carried a Billingsley fluxgate magnetometer (Billingsley TFM100G2), a thermal electron retarding potential analyzer (RPA) [Frederick-Frost *et al.*, 2007], a thermal ion hemispherical electrostatic analyzer, thermal ion RPAs, and the Norwegian multineedle Langmuir probe (mNLP) [Moen *et al.*, 2012; Bekkeng *et al.*, 2010; Jacobsen *et al.*, 2010]. Ongoing analysis efforts include removing the effects of the payload disturbances (sheaths, wake) from the thermal ion measurements of plasma bulk flow and temperature.

The DC magnetic field data presented here are despun from the payload reference frame using a rigid body motion model of the payload dynamics [Horak, 2014]. The model parameters are adjusted to minimize variations in the inertial frame depiction of the angular momentum vector and to minimize variations in the magnitude of the magnetic field other than those driven by altitude. The despun data (**B0 + B1**) are then differenced from an International Geomagnetic Reference Field (IGRF) model (**B0**) to find the deflections (**B1**) caused by auroral currents. The data are smoothed to varying degrees, but are not band-pass filtered, in order to retain the proper phase of the resulting signals.

These in situ instrumentation results are interpreted within the context of an extensive ground-based array of sensors. The instruments specifically used for this study are as follows.

1. A digital all-sky imager at Poker Flat, filtered for the oxygen red and green line emissions (630.0 and 557.7 nm, as seen in Figure 1), and in particular the N_2^+ first negative emission at 427.8 nm, cycling through the three filters on a 12.5 s cadence. Frames from this imager are shown in Figure 1 (first panel).
2. A 47° field-of-view imager, filtered for the first negative emission, operating at 16.4Hz, looking up the field line under apogee at Venetie. The field of view of this imager is indicated by the yellow circle overdrawn on Figure 1 (first panel, a). Frames from this imager are shown in later figures. The noise floor of this camera at full frame rate (16.4Hz) is 300 Rayleighs, and when averaged over 1 s, the noise floor drops to 90 Rayleighs. These levels correspond to equivalent electron energy fluxes of 1.5 mW/m² and 0.5 mW/m², respectively, based on conversion factors of Rees and Luckey [1974] and Strickland *et al.* [1989]. These conversions to energy flux were also used in the Zettergren *et al.* [2014] study.
3. The Poker Flat Incoherent Scatter Radar (PFISR) looking northward over a region encompassing the first two thirds of the trajectory. The PFISR radar was run in a 15-beam mode, allowing observations of large-scale electric fields; a recent analysis tool also extracts large-scale field-aligned currents using PFISR measurements of electric field divergence from the PFISR data as discussed in Appendix A.
4. AMPERE data are also available at high cadence before, during, and after the event [Anderson *et al.*, 2008; Clausen *et al.*, 2012]. The AMPERE data for this campaign are not used for this study but we note the campaign data here as others doing studies on larger scales than our focus may find this data set a valuable connecting point.
5. The Homer Coherent Scatter radar [Hysell *et al.*, 2012].
6. A wide angle Fabry-Perot interferometer (FPI) named the Scanning Doppler Imager (SDI) for monitoring *E* and *F* region neutral winds and temperatures [Conde and Smith, 1998; Anderson *et al.*, 2012a, 2012b].

3.2. In Situ and Camera Observations

Figure 1 shows an overview of the auroral event and the rocket flight. Early in the evening, a quiet evening arc crossed Alaska. A few minutes before the launch, a strong westward traveling surge crossed the launch region. The rocket was launched into the wake of the surge. As indicated in the images, a small active arc crossed the trajectory two times during the flight, labeled here as “arcA” and “arcB.” Between the two times shown, the arc retreated westward and then returned to cross the trajectory the second time.

The keogram in Figure 1 was cut from the medium-field imager along the line of the trajectory and shows the time history of each point along the trajectory (diagonal white line indicates trajectory as a function of time). The crossing of the structure which we will designate “arcA” is indicated just before 5.75UT, and similarly,

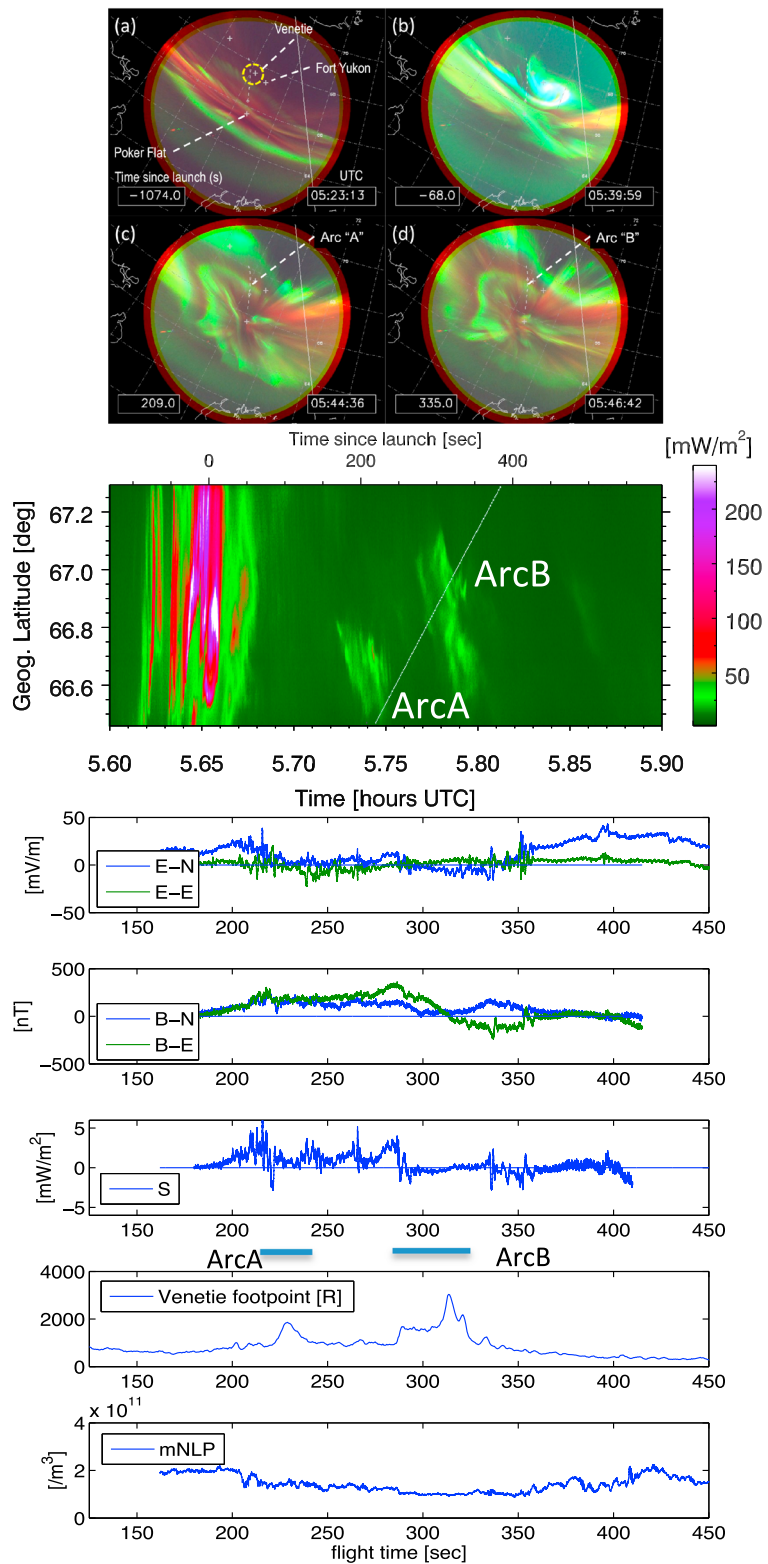


Figure 1. Event overview. Camera data from (first panel) Poker Flat (all-sky images, geographic north upward) and (second panel) Venetie (keogram). The diagonal line on the keogram indicates the payload position. In situ data from the MICA payload. (third panel) Electric and (fourth panel) magnetic fields in geomagnetic coordinates, (fifth panel) Poynting flux calculated from these fields (positive is downward, along the local geomagnetic field,) (sixth panel) Venetie footprint intensity in Rayleighs, and (seventh panel) plasma density as seen by mNLP. The payload reaches apogee of 325.4 km at 297.5s.

the “arcB” crossing is indicated at 5.77UT. Much of the following discussion focuses on the arcB crossing and its poleward edge. The arcB structure in particular will be identified quantitatively in the in situ data by its magnetometer signature indicating a large-scale current sheet.

Figures 1 (third panel)–1 (seventh panel) show the in situ data collected by the rocket payloads along the trajectory. For reference, 233.3s flight time corresponds to 5.75UT; 350s to 5.782UT; and 413.3s to 5.8UT. The in situ data panels show the DC electric field components rotated into a geomagnetic coordinate system; the DC magnetic field deflection from IGRF in the same system; and the Poynting flux calculated from the cross product of those two vectors. Note that the coordinate system used is geomagnetic north (blue) –east (green) –down, so the magnetic field, the Poynting flux, and currents are positive pointing downward toward the Earth surface for this Northern Hemisphere mission. Figure 1 (fourth panel) shows the visible auroral intensity at the magnetic footprint of the moving payload from the Venetie medium-field camera, indicating the locations of arcA and arcB, particularly noting the poleward edge of arcB. After T+320s the foot point exits arcB into a region with a significant drop in auroral activity. Figure 1 (seventh panel) shows the plasma density measured by the mNLP instrument.

The largest-scale features of the density profile are governed by altitude, with the *F* region peaks seen at times T+190 s and T+425 s, and with minimum observed density near apogee at T+325 s. The mesoscale structure indicating a density cavity roughly from T+200 s to T+375 s is consistent with a hysteresis effect in the *F* region driven by the strong electric fields which preceded the recent passage of the westward surge through the region. Zettergren *et al.* [2014] model this behavior and show that the strong frictional heating converts much of the *F* region to molecular ions which then recombine quickly. This process has been shown to leave density gaps in the *F* region for tens of minutes. It is interesting to note that the arcA-B structure forms within the region of low density indicated. It moves within this region, with arcA being its first appearance in the field of view of the medium-field imager, and arcB the second. Between these two times, it retracts westward and then returns back eastward.

The large-scale features of the Poynting flux are worth noting. Throughout the arcA crossing (a visibly structured arc with Alfvénic dynamics that are also seen in the in situ fields data), the observed Poynting flux is directed dominantly into the ionosphere: here energy is coming to the ionosphere both as electromagnetic energy and as particle energy (seen in the visible structures of arcA). In the bright section of arcB, (which is the region indicated both by the bright Venetie footprint and by the large-scale upward current sheet seen by the decreasing B-Eastward as the payload moves north), the Poynting flux is significantly reduced. Here the energy into the ionosphere has been converted to particle energy in the form of the precipitating auroral electrons. One can also describe that this as a reduction of the ionospheric electric field because of the increased conductivity from the precipitation. Poleward of arcB (a region we will examine in more detail in the next figure), the Poynting flux has significant components upward. These small-scale intervals of upward (negative) Poynting flux are the focus of our interest.

Also, note the direction of the large-scale northward component of the electric field: southward before T+340 s, northward after T+350 s. A divergent perpendicular electric field structure like this is to be expected across a downward current region (e.g., equation (1)).

Within the context of the large-scale view given in Figure 1, in this paper we will focus on the smaller-scale in situ signatures seen during the oblique exit of the payload from the arcB structure. Figure 2 details the observations here. The in situ panels show the electric and magnetic field signatures and the calculated Poynting flux over this 100s interval. Two small-scale intervals of downward current (indicated by localized increases in B1-east, as discussed in a later section) are seen at T+337 s and T+352 s. There are regions of upward (negative) Poynting flux all through this interval, close to and between the two DCRs. We will designate these two fine-scale downward current signatures as “DCR-A” and “DCR-B.”

Interpretation of the (single-point) magnetic field data in the context of a current sheet formalism requires a careful examination of the morphology. Figure 3 shows illustrations of the Venetie camera data as the payload moves through the arc edge along a trajectory oblique to the edge.

The camera panels from the medium-field Venetie field site imager (displayed as viewed looking down the field line from above near apogee and rotated here such that geomagnetic north is at the top of the image) show the line of the trajectory and the position of the payload as it moves across (and along) the arc edge. The trajectory is within the Venetie field of view from approximately T+225s to T+375s flight time and is indicated

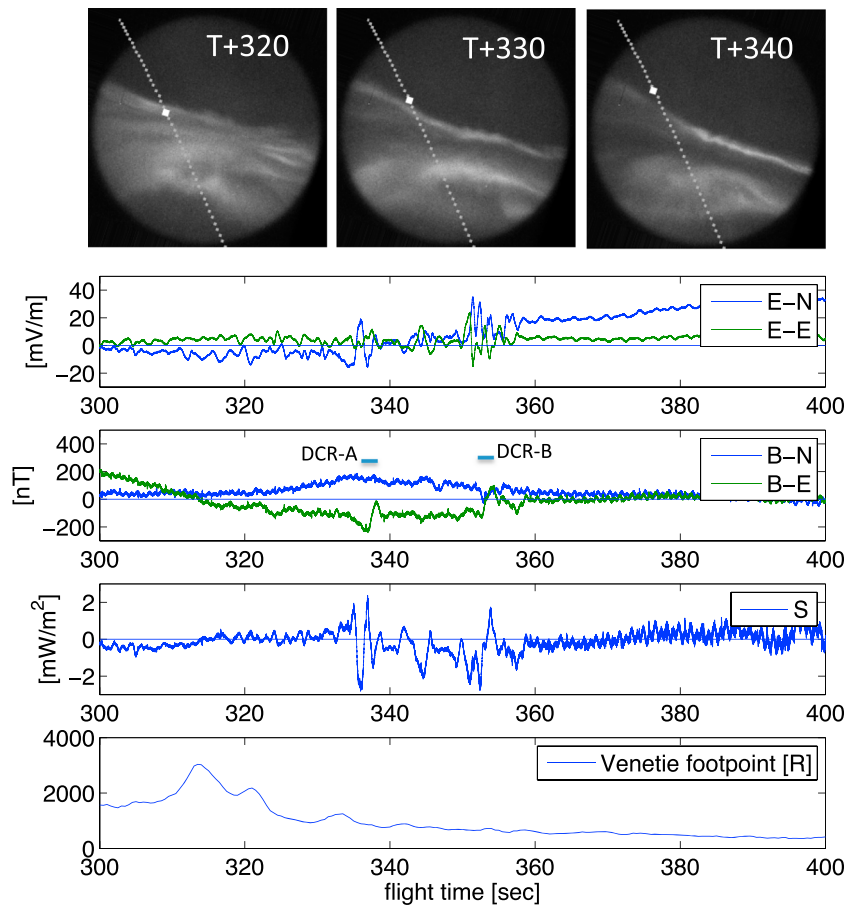


Figure 2. (first panel) Sequence of stills from Venetie field site, looking down the field line with geomagnetic north upward, as the payload moves out of the arcB structure. In situ signatures of (second panel) E, (third panel) B, and (fourth panel) S during this time (S is positive downward, along the local geomagnetic field). (fifth panel) Venetie footprint intensity in Rayleighs.

by a dotted line on the frames, with a marker at the location of the payload footprint in each frame. Note the obliqueness of the trajectory with respect to the current sheet of the arc, which should be considered when viewing the in situ data.

The feather plot in Figure 3 (top left) indicates the direction of the magnetic field deflection vectors (the despun DC magnetic field data minus IGRF) as the payload crosses out of arcB. The axes of the feather plot are relative geomagnetic east and north positions; the vectors are the deflection vector, each with their origin placed at the payload position along the trajectory. Green markers indicate the positions at times T+290, 310, 320, 330, 340, and 350s. The magenta region is arcB; the cyan and red regions are 10 s intervals encompassing the downward current region structures DCR-A and DCR-B.

Early in the crossing, the deflection vectors (which point tangent to the current sheet in an idealized sheet configuration) indicate the arcB current sheet aligned slightly northward of magnetic east. As the payload reaches the edge of the arc, the current sheet turns until it is slightly southward of magnetic east, as does a line defined by the visible arc boundary. Poleward of the arc, the deflection vectors remain parallel to the edge of the arc, tangent to a line slightly south of magnetic east. This remains true and consistent with a sheetlike current structure, through the first of the two strong downward current crossings (DCR-A). The second crossing (DCR-B), however, shows a feather plot image which is not so clearly indicative of a 1-D current sheet crossing.

Figure 3 (bottom) overlays the Venetie footprint brightness (in Rayleighs divided by 10 to share the vertical scale), with the field-aligned current calculated from the curl of the magnetic deflection vector (calculation detailed in section 4). The edges of arcB as defined by these two measurements agree (delimiting the region from T+283s to T+320s), validating our interpretation of the magnetic deflection data through this region

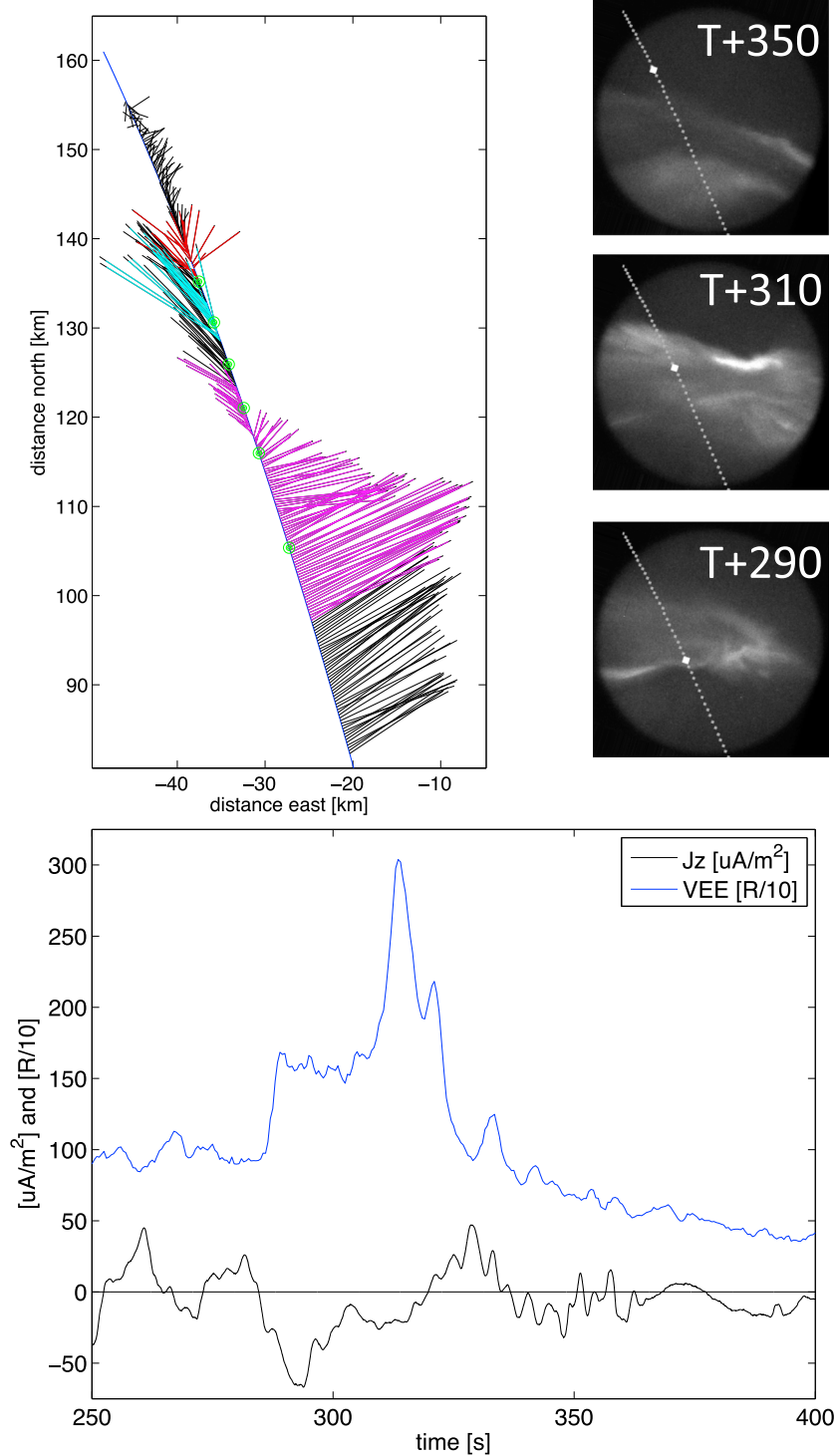


Figure 3. (top right column) The time-dependent poleward boundary of the arcB crossing observed by the Venetie imager (magnetic north upward). (top left) The feather diagram showing the trajectory during the arc edge crossing; the six green markings correspond to the times of the (top right column) six Venetie frames shown here and in the previous figure: T+290, 310, 320, 330, 340, and 350s. (bottom) Comparison of J_z on large scales (black) versus the Venetie (VEE) intensity footprint (blue).

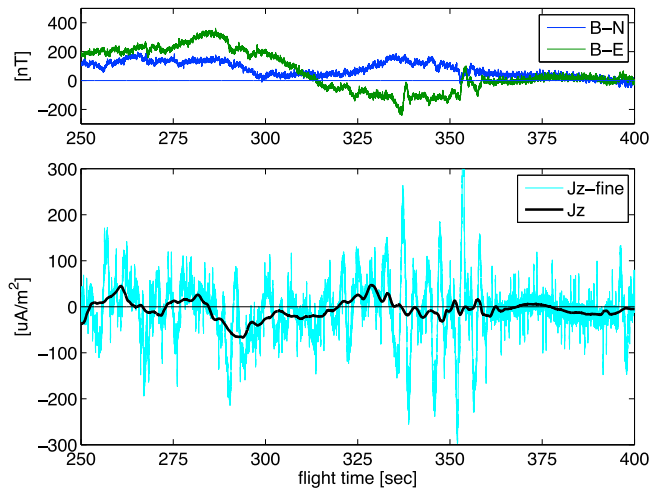


Figure 4. (top) Geomagnetic deflections showing current sheet from arcB, and DCR-A, DCR-B intervals. (bottom) J_z on large and fine scales: black shows large-scale current sheet of arcB, and cyan shows fine-scale DCR structures poleward of it.

with a current sheet picture. Note the location of the peak auroral current signature at T+290s, just as the payload passes into the bright visible structure seen in the T+290s Venetie frame. Separately, it is possible to convert the brightness trace from the imager, into an equivalent precipitating current in the visible arc regions. However, this calculation requires information about the energy structure of the precipitation; while this is available to us in large-scale features (from altitude profiles of the brightness as seen from the Poker Flat imager, as discussed below in the modeling input section), we do not have this information on the fine scales needed here to follow structures within arcB.

4. Data Interpretation and Comparisons

To stitch together the different viewpoints, we make use of a physics-based ionospheric model, driven by inputs derived from the various databases and compared to the metric of the in situ observations. Here in section 4, we discuss (a) the interpretation of the magnetic field data in terms of current sheets and (b) comparisons of the $\nabla \times \mathbf{B}$ and $\nabla \cdot \mathbf{E}$ signatures to each other, first, on large scales and then on small scales. In section 5, we show runs of the *Zettergren et al.* [2014] ionospheric model using ground-based observationally driven inputs assisted by the in situ electric field observations; the output of this model run is then compared against the metric of the in situ magnetic field observations. Our goal here is to describe the observed downward current region signatures in the framework of ionospheric feedback.

4.1. Current Sheet Interpretation

In Figure 3 we have illustrated the morphology of the MICA trajectory and the observed magnetic deflections through the region of arcB, its boundary, and the region just poleward of it, including the two localized features DCR-A and DCR-B. We now quantify these magnetic deflection signatures as current sheets aligned to the principal features of arcB. In Figure 4, we examine the calculation of J_z from the magnetic field data, on two different scale sizes. We are using the magnetometer from the main payload only. In taking the curl from the time history of these measurements, we are assuming that the current is sheetlike, that we are moving obliquely to it, and that it is static over the timescale and spatial scale of the differences required for the curl. We thus calculate J_z as

$$J_z \hat{\mathbf{z}} = \frac{1}{\mu_0} \left(\frac{\partial B_E}{\partial \text{north}} - \frac{\partial B_N}{\partial \text{east}} \right) \hat{\mathbf{z}} \quad (2)$$

where both the magnetic field differences and the position differences are cast in a geomagnetically aligned north-east-down frame. The differences in position and magnetic field components are taken as the payload moves in the northwest direction along the trajectory; as shown in Figure 3, the angle between the trajectory and the arc direction varies from about 20° to about 45°. Here we take the arc direction to be parallel to the current sheet, that is, parallel to the direction of the feathers in Figure 3.

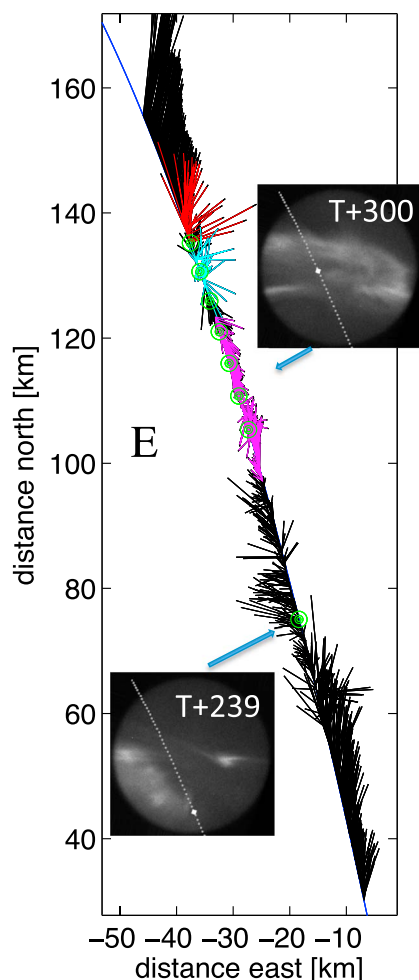


Figure 5. Compare to Figure 3. The in situ electric field signatures in the context of frames extracted from the Venetie camera. The feather diagram shows the electric field vectors in these geomagnetic coordinates along the trajectory; the eight green markings correspond to the times of the six markings of Figure 3 plus the times of the two frames shown here (T+239 and T+300s).

(upgoing ions) have a negative value.) The cyan trace, with lighter smoothing (a one spin period initial window, roughly 1.6 s), oscillates around this signature and also brings out the current density of the localized DCR-A and DCR-B structures which the heavier smoothing cannot see. These localized regions can be interpreted as downward current sheets of several hundred $\mu\text{A}/\text{m}^2$ (positive). An examination of Figure 3 indicates that a current sheet interpretation of DCR-A seems reasonable, in that its deflection vector feathers lie parallel to the nearby large-scale current sheet of arcB; however, DCR-B is not so clearly a localized sheet.

4.2. Comparison of $\nabla \cdot \mathbf{E}$ and $\nabla \times \mathbf{B}$ Signatures

Equation (1) shows that in the auroral ionosphere, current continuity requires relationships between field-aligned currents and perpendicular electric fields. It is interesting to explore the observed relationships between the different terms of equation (1). Figure 3 showed the morphology of the field-aligned current signature as seen in the $\nabla \times \mathbf{B}$ signatures. Figure 5 shows the equivalent signatures in the $\nabla \cdot \mathbf{E}$ data, overlaying a section of the trajectory in geomagnetic coordinates, with the electric field vectors observed in situ at each point along the trajectory. The overview panel of electric field data in Figure 1 shows a large northward electric field outside the region of precipitation (before T+200s and after T+360s); this northward field is consistent with the overall westward flow seen in the neutral winds of Figure A1 (see Appendix A). Here in the feather

The field-aligned current density calculated in this manner is sensitive to the smoothing of the magnetic field data: with minimal smoothing, the data are noisy and the partial derivatives indicate localized deviations; with heavier smoothing, the larger-scale current sheets can be seen but not the small-scale ones. Figure 4 illustrates these smoothing effects for arcB and its poleward region, showing the different features observed at different scale sizes. Figure 4 (top) shows the geomagnetic north (blue) and east (green) components of the deviation of the measured magnetic field from IGRF. The current sheet associated with arcB is seen as the large smooth decrease in B_E from T+285s through T+315s (as the payload moves through the sheet to the northwest). Poleward of this, at T+337s (DCR-A) and T+354s (DCR-B), two sharp increases in the same component are seen, qualitatively interpretable as localized current sheets of opposite sign to the main sheet.

Figure 4 (bottom) shows the field-aligned current calculated from equation (2) with two different choices for smoothing the magnetic field data. The smoothing is done using an unweighted moving average. The black trace, using a heavy smoothing of the despun magnetic field data (the data are smoothed with a window of six spin periods, roughly a 10 s interval, before calculating the curl which is then again smoothed over a shorter interval), illustrates the 10–50 $\mu\text{A}/\text{m}^2$ (negative) current density of the precipitation electrons of arcB. (J_z is positive downward in this coordinate system, such that currents from precipitating electrons

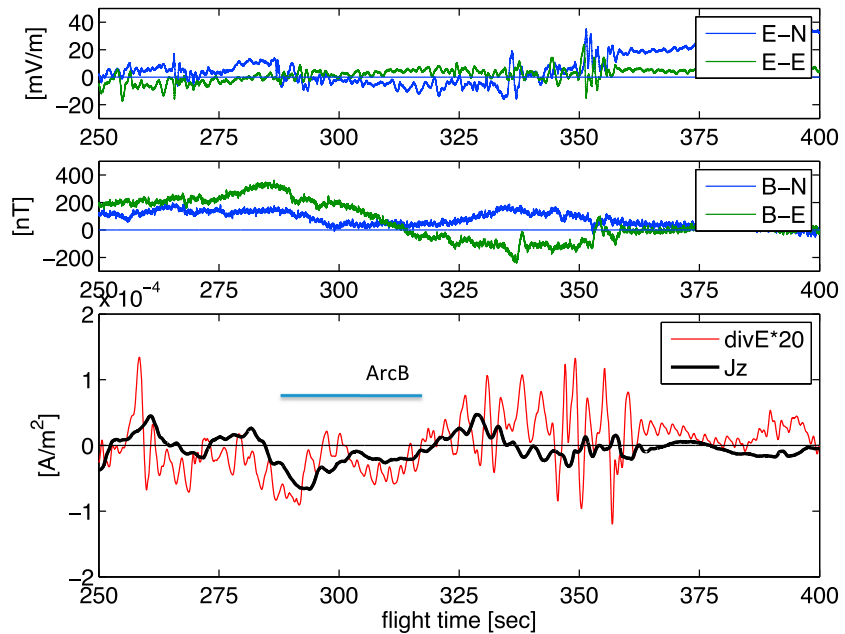


Figure 6. (top panels) In situ \mathbf{E} and \mathbf{B} . (bottom panel) Large-scale comparison of calculated quantities J_z and $\nabla \cdot \mathbf{E}$. Black is J_z (now in A/m^2); red is $20 \nabla \cdot \mathbf{E}$.

diagram, we see this northward electric field at the bottom and top of the trajectory section, interrupted by the activity of arcA and arcB. At T+239s, the payload crosses to the west of the brightest occurrence of arcA, as indicated in the inset image. At that time, marked by the lower green marker in the feather plot, the electric field points westward and a bit northward, pointing toward the nearby bright arc. Further on, at T+300s, the payload is in the center of the arcB activity. The inset image is from the time at the center of the purple region in the feather diagram. Southward of the center of the purple region (arc B), the electric field points northward; northward of it, the field points southward; again, along the trajectory, the electric field points toward the nearby bright arc. This is an illustration of the requirement from continuity that the divergence of \mathbf{E} must balance the curl of \mathbf{B} ; that is, the electric field converges toward a region of precipitating electron current.

Similar relationships are explored in *Lanchester et al.* [1996]; here we explore this relationship quantitatively using equation (1). The statement that the electric field vector points toward the brightest spot in a nearby arc can be quantified by comparing the $\nabla \cdot \mathbf{E}$ with the $\nabla \times \mathbf{B}$, related as per equation (1). In Figures 6 and 7, we compare \mathbf{E} , \mathbf{B} , $\nabla \cdot \mathbf{E}$, $\nabla \times \mathbf{B}$, and the observed (F region) plasma density from the onboard mNLP, on two different scales, again noting the different features which can be observed on large- and small-scale sizes. As with the $\nabla \times \mathbf{B}$ calculation described above, the $\nabla \cdot \mathbf{E}$ calculation uses the electric field components in geomagnetic coordinates and calculates the gradient using spatially separated points along the payload trajectory. Again the field data are smoothed before (and after) the calculation, to different levels for large- and fine-scale features; the windowing used is the same as for the $\nabla \times \mathbf{B}$ calculations described above.

Figure 6 shows, on large scales, that the main region of arcB as delineated by the current sheet (from T+280s through T+315s) can be described as a region of precipitation (the field-aligned current) into a region of roughly constant conductivity. The black curve of Figure 6 (bottom) shows the large-scale J_z of Figure 4, overlaid with a red curve which is the first term of equation (1) using $\Sigma_p = 20$ mhos. The field-aligned current is from an external source, and the observed perpendicular electric field is consistent across arcB with the current continuity equation. The choice of $\Sigma_p = 20$ mhos was made to roughly match the two terms; if the value found by the model (described in the next section, and used in Figure 11) of about 7 mhos were used instead, it would reduce the red curve proportionally.

Figures 7 (first panel)–7 (third panel) consider this same comparison, now on fine scales, in the region poleward of arcB. In this region, $\nabla \times \mathbf{B}$ and $\nabla \cdot \mathbf{E}$ are related by a conductance value of only 4 mhos; it is reasonable that the conductivity here is lower since this is a region without active precipitation. Note that this value is consistent with the modeled conductivity at this time.

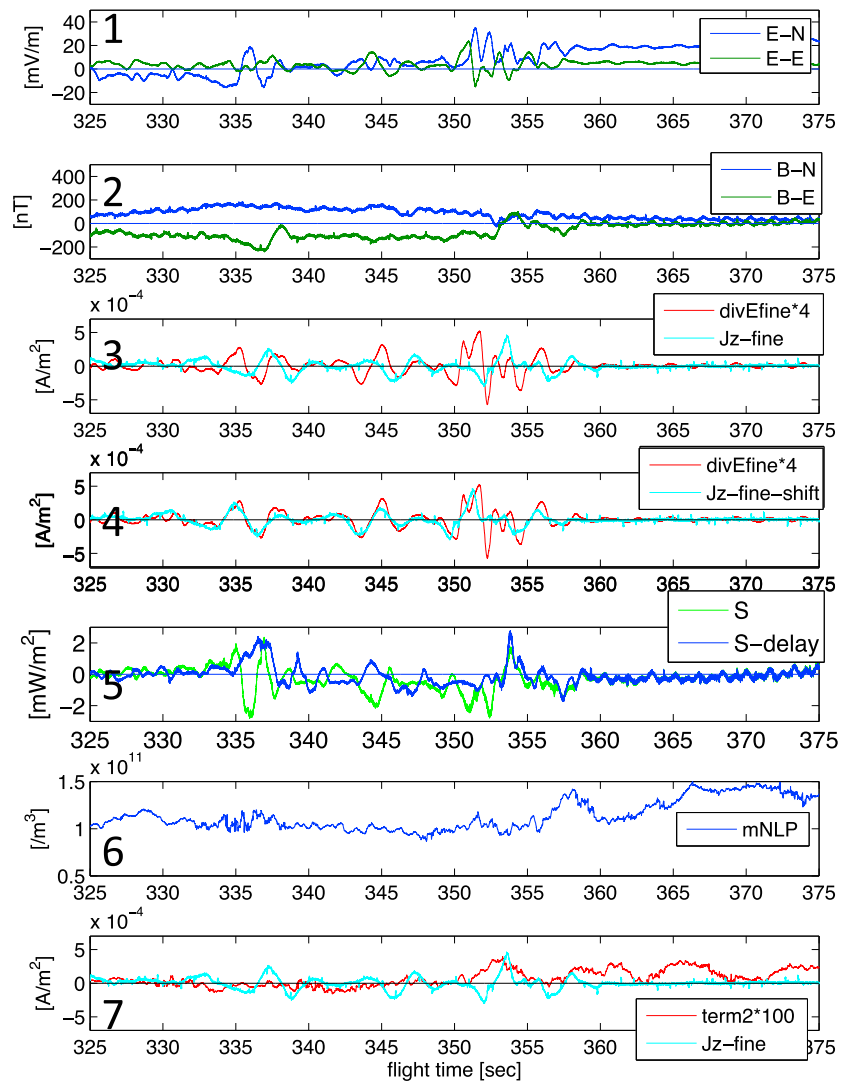


Figure 7. Fine-scale comparison of calculated quantities J_z and $\nabla \cdot \mathbf{E}$. (third and fourth panels) Cyan is J_z ; red is $4 \nabla \cdot \mathbf{E}$. The fourth panel compares J_z and $\nabla \cdot \mathbf{E}$ on fine scales, but with a shift in the time axis to align the magnetic and electric fluctuations. (fifth panel) This compares the Poynting flux S to the construction S_{delay} discussed in the text. (sixth panel) F region plasma density; note the position of the electric field fluctuations with respect to local increase in plasma density. (seventh panel) This compares the fine-scale J_z to the term in equation (1) involving conductance gradients.

It is interesting to note the clear fine-scale correlation which can be seen in Figure 7 (fourth panel), in which the observed $\nabla \times \mathbf{B}$ structure has been shifted to the left by 2.35s. With this shift, these downward current structures appear just as electrostatic (in their relationship to $\nabla \cdot \mathbf{E}$) as does arcB itself, except for the finer-scale oscillations in \mathbf{E} seen in DCR-B, discussed below. While it is true that the electric field instrument is on one payload and the magnetic field instrument is on another, they are quite close to each other and their observations should be shifted by a few tenths of seconds at most. One possibility for the apparent spatial shift between the electric and magnetic signatures here may be the proper motion of the arc structures. *Mallinckrodt and Carlson* [1978] illustrate how proper motion can cause a displacement between otherwise related field signatures. The delay seen here is consistent with an Alfvén speed along the field line of 1000 km/s and a proper motion of 1 km/s, assuming that the electric field is impressed on the flux tubes at 100 km altitude and the observation is 200 km above that.

Another possible explanation for this shift in signatures may be the ionospheric Alfvén resonator [*Lysak*, 1991; *Chaston et al.*, 2002; *Lysak and Song*, 2011], which causes phase mixing and phase shifting in electric and

magnetic field activity. The timescales of the IAR are only a few seconds, so it is possible that arcB and its current systems illustrate the phase shifting seen within these lower ionospheric structures.

Given the apparent shift between the fine-scale electric and magnetic signatures, we revisit the Poynting flux calculation. If the shift between the electric and magnetic field signatures is caused by a proper motion or a phase shift, as discussed above, we can consider the Poynting flux vector which would be observed at the altitude where these signatures originate. We take as a premise that where the signatures originate is somewhere below the observation, in the E region, and that at this point the divergence and curl signatures overlay as in Figure 7 (fourth panel). We define the Poynting flux that would be observed at that point as S_{delay} and calculate $\mathbf{E} \times \mathbf{B}$ with the electric field shifted forward by the same 2.35 s. Figure 7 (fifth panel) compares this S_{delay} (blue) to our local calculation of the observed S at the payload (green). Compared to the unshifted S , we see now that the bulk of the Poynting flux in the downward current regions is still inward toward the ionosphere as it should be (positive S_{delay} , T+336 s, T+354 s) but that the finer-scale oscillations (T+354 to T+357 s, discussed below in the context of ionospheric feedback) are apparently sourced by the ionosphere and are sending Poynting flux energy up the field line (negative S_{delay}).

Finally, we consider Figure 7 (seventh panel). Here we consider the conductance gradient source term of equation (1). Consider the relationship between the first panel (the electric field fluctuations) and the sixth panel (the F region plasma density) of this figure; notice that the downward current region structures and associated electric field signatures are located just inside the boundary of the low-density region noted in the discussion of Figure 1. We wish to consider whether an E region conductance gradient below the observed F region density gradient (seen from T+350s to T+360s) could be responsible for the presence of the downward current structure in that region. Figure 7 (seventh panel) compares the field-aligned current density (again shown in cyan), to the $(\nabla_{\perp} \Sigma_p \cdot \mathbf{E}_{\perp})$ term of equation (1). We use

$$\sigma_p = n_{\text{plasma}} M v_{\text{in}} / B^2 \quad (3)$$

to estimate the Pedersen conductivity σ_p from the plasma density n_{plasma} in the F region (given this way by Kelley [1989], where M here is ion mass, v_{in} is the ion-neutral collision frequency, and B is the magnetic field strength) and multiplied by 250 km as an estimated slab width for this F region conductance. This equation is valid for altitudes where the ion-neutral collisional frequency is nonzero but the ratio of ion gyrofrequency to collision frequency is still large (above 130 km) [Kelley, 1989]. We also use the relatively constant value of \mathbf{E} seen beyond T+360s for this calculation, since we are interpreting the oscillatory signals as a result, not a cause, of this feedback. In Figure 7 (seventh panel), we consider how much stronger the conductance gradient needs to be to source the observed field-aligned current density; it requires a multiplier of 100. However, our derived conductance represents that contributed by the F region, and the conductance gradient which generally most contributes to the field-aligned current term would be from the E region (where the collision frequency and gyrofrequency are approximately equal). Thus, the observed F region conductance gradient is insufficient by a factor of 100; since the mobility in the E region can be considerably higher, the E region conductance (and therefore gradient) could provide the required driver for originating this downward current. We will see in the modeling section below that the model does not capture a strong E region gradient at this location. At the time of the observation shown in Figure 7, the divergence of the \mathbf{E} term contributes much of the field-aligned current, as indicated in the plot. Still, it remains a point of interest that DCR-B (which, unlike DCR-A, is not immediately adjacent to the significant energy flux associated with arcB) sits just inside the edge of the larger-scale density cavity which was thought to have been caused earlier by the passage of the westward surge.

5. Ionospheric Modeling Case Study: The MICA Event

An ionospheric model is used in this section to synthesize and compare various observations from MICA, PFISR, and camera instrumentation. This exercise provides an opportunity to validate the model, examine various assumptions used in the modeling and data analysis (electrostatic, etc.), and assess different contributions (neutral winds, electric fields, and conductance structures) to the observed field-aligned currents.

5.1. Model Description, Data Preparation, and Configuration

A variant of the model developed by Zettergren and Semeter [2012] has been used to interpret density and heating signatures observed by PFISR during the MICA experiment [Zettergren et al., 2014] and is

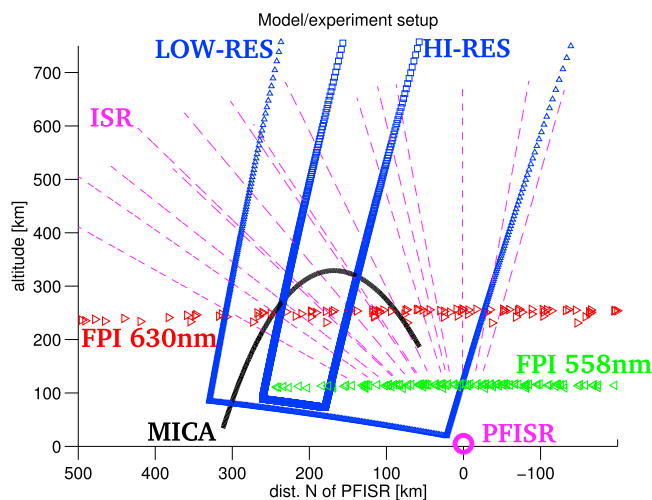


Figure 8. Data sets used to specify model boundary conditions and source terms. This perspective represents a view from the west of PFISR, which is represented by the magenta circle near the origin of the coordinate system. Dashed lines show the beam positions for the PFISR experiment. Red and green triangles used for the FPI (SDI) neutral wind data represent individual observation locations within the field of view, and blue triangles used with the model mesh outline show the centers of each cell and illustrate grid spacing for the two resolutions.

leveraged, in this section, to study field-aligned currents around arcB. This model self-consistently couples a two-dimensional multifluid model (conservation of mass, momentum, and energy) of seven ionospheric species to an electrostatic treatment of auroral currents. All important ionospheric plasma and heat sources (impact ionization, thermal electron heating and inelastic cooling, thermal conduction, and thermoelectric heat fluxes) are included in the code. High-altitude proton dynamics and photoionization [Solomon and Qian, 2005] are also included in the model. The model uses generalized, orthogonal curvilinear coordinates [Zettergren and Snively, 2013; Zettergren et al., 2014]. For the MICA study, we use a dipole coordinate system [e.g., Huba et al., 2000] in which one dimension (denoted x_1) runs along the geomagnetic field lines and the other in the direction of increasing L shell number (denoted x_2). Resolutions for the simulations presented in this paper are as high as $\Delta x_1 \times \Delta x_2 = 500 \text{ m} \times 160 \text{ m}$ in the E region, a much finer resolution than that used in the companion paper to this study [Zettergren et al., 2014]. The model equations and numerical methods have been described in Zettergren and Semeter, 2012 [2012, equations (1)–(5) and (20), and section 2.6]. The model is comparable to many other existing codes [Huba et al., 2000; Noël et al., 2000, 2005; de Boer et al., 2010] and is used here in a configuration (boundary conditions, etc.) similar to that in our study of the ISR data from the MICA campaign [Zettergren et al., 2014].

Figure 8 illustrates the relationships of different data sets used to specify model boundary conditions and source terms. This perspective represents a view from the west of PFISR, which is represented by the magenta circle near the origin of the coordinate system. Dashed lines show the beam positions for the PFISR experiment. Red and green triangles used for the Fabry-Perot interferometer (SDI) neutral wind data represent individual observation locations within the field of view, and blue triangles used with the model mesh outline show the centers of each of the outer boundary cells and illustrate grid spacing.

Electric fields for our high-resolution modeling study are taken from MICA measurements, which are interpolated onto the model grid, smoothed, scaled to the top boundary, and then integrated to produce a potential versus L shell profile. This potential is held fixed for the duration of the simulation.

Neutral wind fields for the high-resolution modeling study are taken from SDI data as described in Zettergren et al. [2014]—a single altitude profile is used for the entire grid. The winds are, thus, horizontally homogeneous for the simulations presented in this study and are also held fixed in time.

Particle precipitation inputs for the high-resolution runs are derived from medium-field imager data from the Venetie station. The characteristic energy of the precipitation is derived by determining the best match between the altitude profile of the N2+ 427.8 nm emissions measured from the Poker Flat all-sky camera to emission profiles computed by the Lummerzheim and Liliensten [1994] electron transport model for

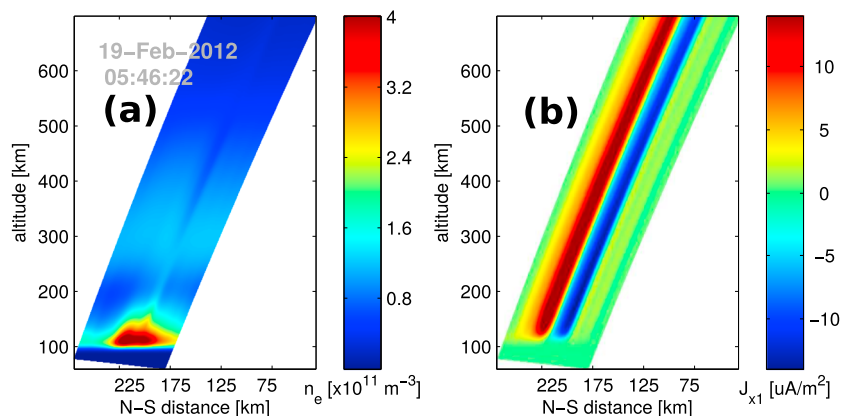


Figure 9. Modeled densities and currents during the rocket traversal of arcB for the simulation with heavily smoothed inputs. (a) Electron density and (b) field-aligned current. This particular output frame corresponds to 5:46:22UT in the simulation.

a range of Maxwellian fluxes. Calibrated 427.8 nm column integrated intensity of the Venetie camera and this characteristic energy are then used to specify total energy flux using the relations reported in *Rees and Luckey* [1974].

Initial conditions for the high-resolution model runs are extracted from the simulations presented in *Zettergren et al.* [2014]. Namely, their 5UT event simulation [*Zettergren et al.*, 2014, section 3.3] results for densities, temperatures, and drift velocities at time 5:42UT are interpolated onto the high-resolution mesh used in this study to start the new simulations. The 5UT simulation from *Zettergren et al.* [2014] incorporated PFISR electric fields and precipitation derived from the Poker flat all-sky camera system and SDI data in the minutes leading up to the substorm surge. Hence, the initial condition for our simulations correctly incorporates the plasma state due to frictional heating and precipitation occurring prior to the rocket flight. Two different model runs are presented in this paper, one with the input data (fields, total energy fluxes) heavily smoothed and one with only a moderate level of smoothing.

5.2. Model Results

Representative results from the simulations are first presented to provide context for the remainder of the simulation results and show the modeled two-dimensional structure of the current system that is the primary subject of this paper. Figure 9 shows a frame of output from the model, extracted as the rocket is passing out of the arcB upward current region and into the adjacent dark region (\sim 5:46:22 UT). This frame was extracted from the heavily smoothed simulation. The region of intense precipitation seen in Figure 9a is coincident with a negative field-aligned current (an upward current) in Figure 9b. Poleward of this upward current region, there is a spatially extended region of downward current and the transition between the upward and downward current channels occurs over a very short cross-field distance.

For purposes of comparing the simulation results with in situ data, the output is interpolated in space and time onto the rocket path (sampled at 1 s time resolution). This is accomplished by first spatially interpolating each frame of output from the model (representing an instant in time) onto the rocket trajectory, effectively forming a keogram from the model results. After this step, the model output is interpolated in time by selecting the parameter of interest (electron density, currents, etc.) from the location in each frame nearest to the rocket position at that time. The result of this process is a time series of model output representing what the rocket would measure if it flew through the model ionosphere. Given the nature of coordinate system transformations and model output rate (at 2 s cadence), a nearest-neighbor interpolation in both space and time is used. This results in some coarseness to the plotted parameters, but all features are well resolved and smooth in the model's native coordinate system and time basis (e.g., Figure 9).

Figure 10a shows input electric fields and output field-aligned current (FAC) densities (Figure 10b) for both simulations. Figure 10b demonstrates qualitative agreement of the model results with the FAC data originally presented in Figure 3 and repeated in this panel as the light grey line. In particular, the upward and downward

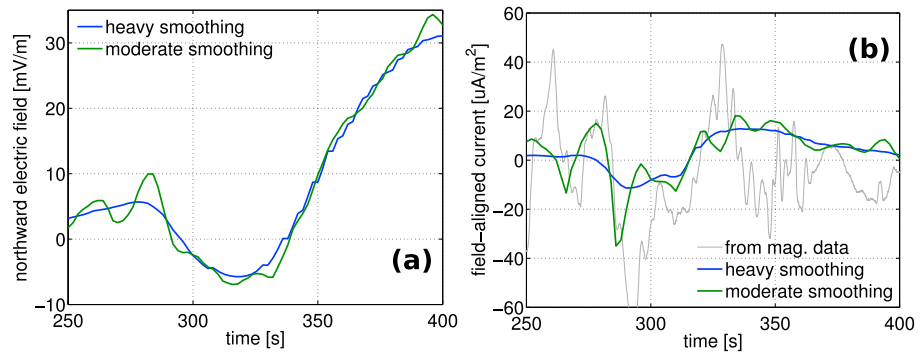


Figure 10. (a) Driving electric fields and (b) output field-aligned current sampled along the MICA trajectory for two cases with different levels of smoothing: heavily smoothed inputs and moderately smoothed inputs. In Figure 10b, the large-scale current densities J_z estimated from the magnetometer data on MICA have been repeated for comparison.

current channels line up in time with those in the data and are consistent with the observed Venetie intensity and total energy flux; i.e., the energy flux is large in the upward current region and small in the downward current region (note in particular the transition from upward to downward J_z near T+320). As seen in Figure 10b, the simulation with heavily smoothed input electric fields exhibits consistently lower FACs ($\pm 12 \mu\text{A}/\text{m}^2$) than those observed by MICA ($\pm 50 \mu\text{A}/\text{m}^2$). The simulation with less input smoothing brings the FAC intensity (for this run $-35 \mu\text{A}/\text{m}^2$ to $18 \mu\text{A}/\text{m}^2$) more in line with the MICA data, but is still consistently lower than what the in situ observations suggest. The simulation with moderate smoothing shows varied FAC structures before 275 s, which are not apparent in the data. However, the generally favorable agreement between the arcB upward and downward current regions in the data and simulations ($275 \leq t \leq 375$ s) invites further, more detailed analysis of the model output.

The contributions of various thermospheric/ionospheric processes to the observed and model field-aligned current can be evaluated using detailed output from the high-resolution model run. Equation (1), sans Hall terms and with addition of dynamo neutral wind-driven currents becomes

$$J_{\parallel} = \Sigma_p(\nabla_{\perp} \cdot \mathbf{E}_{\perp}) + \nabla_{\perp} \Sigma_p \cdot \mathbf{E}_{\perp} + \nabla_{\perp} \cdot (\Sigma_p \mathbf{v}_{n,\perp} \times \mathbf{B}). \quad (4)$$

The Hall terms are neglected as the term $\hat{\mathbf{e}}_1 \times \mathbf{E}_{\perp}$ lies in the zonal direction in our model (since the electric field is mostly in the north-south direction). This implies that the Hall term then is dominated by the zonal part of the Hall conductance gradient, which we are unable to resolve in the 2-D simulations (or, for that matter, in the rocket results). Likewise, we neglect the Hall portion of the neutral wind current divergence term. This equation presumes a local Cartesian coordinate system with the magnetic field along the x_1 direction.

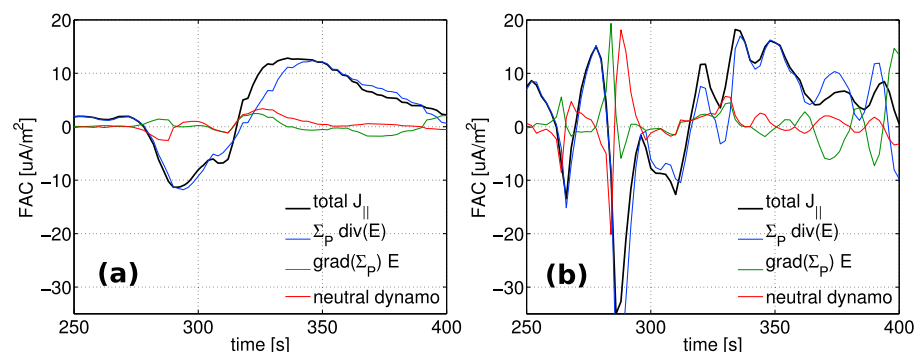


Figure 11. Contributions of different terms to field-aligned current density. Panel a: heavily smoothed simulation. Panel b: simulations with moderate smoothing.

In the dipole coordinate system used by the model, each term in a field-integrated equation takes on a slightly different form, i.e.,

$$J_{\parallel}(x_{1,\min}) = \frac{1}{h_2(x_{1,\min})h_3(x_{1,\min})} \left\{ \int_{x_{1,\min}}^{x_{1,\max}} h_1 h_2 h_3 (\sigma_p (\nabla_{\perp} \cdot \mathbf{E}_{\perp})) dx_1 + \int_{x_{1,\min}}^{x_{1,\max}} h_1 h_2 h_3 (\nabla_{\perp} \sigma_p \cdot \mathbf{E}_{\perp}) dx_1 + \int_{x_{1,\min}}^{x_{1,\max}} h_1 h_2 h_3 \nabla_{\perp} \cdot (\sigma_p \mathbf{v}_{n,\perp} \times \mathbf{B}) dx_1 \right\}. \quad (5)$$

where the h_i parameters are metric factors for the dipole coordinate system [Huba *et al.*, 2000], and $x_{1,\min}$, $x_{1,\max}$ represent the field-aligned coordinate at the logical bottom and top of the mesh, respectively. Each term in equation (5) is readily identifiable with a corresponding term in equation (4) and provides a means to use the model output to break the field-aligned currents down into various contributing terms. Finally, it is noted that terms in the field-line-integrated equations (4) and (5) should, in situations examined here, be fairly accurate representations of field-aligned current. The modeling conducted in this study encapsulates only the apogee portion of the flight, and since there is very little current closure at or above these altitudes, a field-integrated equation suffices.

Different terms which contribute to the field-aligned currents are plotted in Figure 11 for the simulation with heavy smoothing (Figure 11a) and the simulation with moderate smoothing (Figure 11b). For the heavily smoothed simulation in panel Figure 11 the electric field divergence term dominates the FAC for most of the flight. The exception is the entry into the DCR around 315s, where the total current is about 5–7 $\mu\text{A}/\text{m}^2$ and all of the current terms are contributing a roughly equal amount. It is worth noting that the wind FAC contribution in equation (4) could be broken into a divergence term and a conductance gradient term. The divergence term, however, is unimportant since the wind fields were assumed to be horizontally homogenous. Hence, the wind terms are seen to be significant in Figure 11a in the same regions where the conductance gradients exist. The gradient terms are only important right at the transition from UCR to DCR, while the electric field divergence is, again, the dominant contributor in the center of these current channels and, indeed, through most of the flight. The simulation with lesser smoothing of data inputs yields similar conclusions. The electric field divergence term dominates along the flight path, except for the DCR/UCR border where the winds and conductance gradients contribute significantly. Two of the maxima in the downward FAC, one at ~ 325 s and the other at ~ 335 s, have significant gradient/wind contributions, but the latter is dominated by the gradient effects. The final downward FAC maximum, at ~ 345 s, is apparently entirely due to electric field structure. One other notable feature in this plot is that the wind terms (which are controlled by conductance gradients as discussed above) and the conductance gradient terms are opposite prior to 300s and then of the same sign during the UCR/DCR transition. This is due to the fact that the winds are predominantly antizonal (35m/s magnetic north, -150 m/s magnetic east), which contributes an effective field $\mathbf{v}_{n,\perp} \times \mathbf{B}$ of about 7mV/m in the southward direction. Prior to 300s, the electric field is mostly northward and small (< 10 mV/m, see Figure 10), and the winds largely counteract its effects. After about 295s, the electric field transitions to southward and then acts in concert with the winds.

6. Discussion and Conclusions

6.1. Summary of Data and Implications

In this paper we have presented a case study illustrating the contribution of ionospheric conductivity gradients in generating auroral return currents. Large-scale upward FAC structure within a 20 km wide upward current region is observed in situ to have a gradient scale length of 7.5 km. The edge of the associated visible precipitation activity is traversed over a gradient scale length of 5 km in the geomagnetic north/south direction at both the equatorward and poleward edges. In the nearby downward current region, the observed current signatures are narrower, with widths in δB_E of 1 km and gradient scale lengths in J_z of 0.5 km. The modeled upward currents have similar scale lengths as the observed (10 km versus 7.5 km), but the modeled DCR is wider than the observed. The modeled conductance gradient scale length at the poleward edge of arcB is 30 km, interestingly wider than that of the precipitation edge (which is smoothed in the model inputs from 5 km to 13 km); this additional width may contribute to the comparatively large width of the modeled DCR.

We can compare the divergence of \mathbf{E} as calculated from two different perspectives: directly from the PFISR data and directly from the in situ measurements. Figure A1d in the Appendix shows the PFISR calculation from

the time when the payload is leaving arcB. Following the trajectory of the payload roughly up the center of this panel from Poker Flat to approximately 68° , PFISR data show a region of precipitation roughly 1.5° of latitude (165 km) across, followed by a downward current region roughly 0.5° of latitude (55 km) across. These widths are considerably larger than the 20 km width of arcB and the 18 km region containing the various downward current signatures seen by the in situ measurements. Correspondingly, the calculated divergence of \mathbf{E} is smaller for the PFISR calculation: roughly (positive or negative) 10^{-6} V/m², compared to in situ observations (see Figures 6 and 7) of 2×10^{-5} V/m² in the upward current region and 10^{-4} V/m² in the downward current region.

6.2. Ionospheric Feedback

The in-situ-observed downward FAC region additionally has smaller-scale structure overlaid in its electric field signatures. Interpreted as spatial structure, the electric field in DCR-B has roughly four oscillatory cycles covering 2.5 km of north-south distance, overlaid on and equatorward of (or centered on if shifted as in Figure 8) the DCR-B magnetic field structure (1 km wide). The single-point observations cannot unravel these signatures, nor can the electrostatic model. A plausible explanation for these Alfvénic signatures (with, as noted in Figure 8, upgoing Poynting flux) is ionospheric feedback from conductivity gradients below the observation point, as exemplified in the models of *Russell et al.* [2013] and *Lysak and Song* [2011]. Our model does not capture a conductance gradient at this DCR-B location (unlike that of DCR-A, which sits closely on the precipitation edge of arcB) but we note in the observations that this is the location of the exit from the original large-scale density cavity.

We suggest that the oscillatory electric field structures in the downward current regions here are an example of the ionospheric feedback mechanism proposed by *Russell et al.* [2013]. These fine-scale electric field structures can be a source of upgoing Poynting flux generated by the ionosphere, as seen in the negative values of S_{delay} in Figure 8. In order to model and quantify the effects and significance of such feedback, models and observations need to capture scale sizes of 1–5 km for the drivers and roughly one quarter of that for the response.

6.3. Summary of Model Results and Data Comparison

Model results outlined above, which were generated using data to specify initial and boundary conditions, indicate that the conductance gradient at the poleward edge of arcB contributes significantly to FACs—as much or perhaps more so than the electric field divergence. Conductance gradients such as this are particularly critical to current continuity considerations since they also factor into neutral dynamo calculations. Specifically, the conductance spatial structure appears twice in equation (4), once for the electric field term and again in the neutral wind term. If the winds and fields are sympathetic, as appears to be the case for our arcB exit, these contributions are additive. Insofar as our wind estimation and interpolation are accurate, neutral wind contributions to current density are similar to those of the ~ 5 mV/m electric fields measured around the arcB UCR to DCR transition. While our wind estimation encodes many assumptions, i.e., much interpolation and averaging, we have demonstrated a plausible interaction between dynamo winds and small-scale auroral conductance features. Ionospheric conductivity structures, and thermospheric winds have impacts that likely need to be taken into account in models of small-scale magnetosphere-ionosphere coupling—including those that are time dependent. With regard to implications for magnetosphere re-ionosphere interactions involving Alfvén waves (the time-dependent problem not specifically addressed in the above modeling), conductance structures represent variations in reflection coefficient over small scales and serve as a source of neutral wind-generated Alfvén waves to the magnetosphere.

Our data and analysis have yielded the following conclusions and interpretations:

1. The basic arc-scale-size features of even a small (tens of kilometers) transient (tens of seconds) arc such as arcB can be electrostatic. ArcB is traversed by the payload in 20 km of geomagnetic northward motion, and its accompanying DCR structure spans an additional 18 km. The transition from upward to downward current regions occurs over only a few kilometers of geomagnetic north distance. Each of these features is well described by electrostatic terms.
2. The downward current region just poleward of the visible arcB does contain, in addition, Alfvénic Poynting flux and current structure. The downward current sheets (which appear electrostatic) are a few kilometers in width; the overlaid Alfvénic signatures have an apparent spatial wavelength (assumed spatial here because of our single-point measurements) of approximately 1 km. The upgoing Poynting flux which can be attributed to this Alfvénic activity is small and, at the observation point, reduced by phase mixing

or other propagation delays. However, the location of this activity with respect to preexisting large-scale density structures points to the importance of ionospheric feedback as a driver for initiating auroral coupling regions.

3. Arc edge effects are significant in the current continuity relationships seen by both the data and the modeling.
4. It is plausible that the neutral winds are playing a significant role in field-aligned currents in regions of strong conductance gradients.

6.4. Implications for Multipoint Mission Design

One motivation for this study, beyond the characterization of this particular auroral event, concerns the design of future multipoint in situ auroral missions and magnetosphere-ionosphere coupling models. What is the minimum energy-significant gradient scale length in the auroral ionosphere? Significant for what processes? What are the in situ observed scales for these processes for which remote sensing can only provide a proxy for modeling? Multipoint missions are designed to study spatial structuring; determining the spatial-structure-scale sizes of interest in the auroral ionosphere is in itself an interesting science question. On the modeling side, to what level of accuracy do local ionospheric models properly simulate the response to different spatial structuring in this driving? We wish to examine the sensitivity of the ionospheric response to forcing specified with finer and finer spatial detail.

Let us consider then the implications of this MICA event study, for the design of a multipoint in situ ionospheric mission to investigate magnetosphere-ionosphere coupling. The MICA study was done without in situ auroral precipitation measurements: the auroral precipitation effects were inverted from the imagery. The energy flux and characteristic energy maps generated from the imagery, together with the electric field information from the in situ observations, were sufficient to drive the model to generate a modeled current structure similar to that which was observed in situ. Either in situ electric field data, or field-aligned current information, is needed in addition to the energy flux information, to generate this picture. For MICA, our camera array was insufficient to properly extract field-aligned current information from the visible signatures; the current inversion calculation is very sensitive to the energy of the incoming particles in a way that the energy flux inversion calculation is not. Thus, we used the in situ electric field information to drive the model. A more capable camera array [Dahlgren *et al.*, 2015] could generate a map of (upward) field-aligned current sufficiently to drive the model, but this would be greatly aided by assimilation with in situ electric field observations. Observations of in situ density structuring provide additional constraints, but the dominant conductivity effects are observable from the inverted imagery, using assimilative techniques. A multiple-point mission seeking to unravel coupling processes, will need to include rigorous ground-based imagery together with either in situ electric or magnetic field data. The separation scales between the observation points would need to be less than 1 km in order to quantify both electrostatic and Alfvénic features. For our MICA study, the single-point observations, and the electrostatic model, cannot definitively interpret the Alfvénic signatures which overlie the electrostatic features.

A modern ground-based imager array with the capability to invert energy flux and characteristic energy maps from imagery can provide the necessary context for assimilation of an array of low resource in situ observations. The combination of assimilated data with modeling techniques provides information about unobserved parameters of the ionosphere system. Such a multipoint mission would allow a quantitative observational study of the effects of auroral structuring on M-I coupling, which could be used then to quantify subgrid responses in larger-scale coupling models, as is needed by M-I coupling simulations working to capture the effects of ionospheric response and feedback.

Appendix A: PFISR Observations of Fields and Currents

For comparison to a larger-scale view, we include an analysis of the coincident PFISR data. PFISR was operated in a 15-beam pattern (see Figure 9). The signatures which can be examined with these data have large gradient scale lengths and long time constants. The plasma flow field data from PFISR can be used to calculate the electric field in different ways. A 1-D calculation assuming variations only in the latitudinal direction can provide a line of electric field vectors along the central axis of the PFISR beam field [Heinselman and Nicolls, 2008]; two examples of this calculation are shown in Figures A1a and A1b. Alternatively, the line-of-sight flow field observations can be assimilated into a computational field in two dimensions, and its divergence can be calculated [Nicolls *et al.*, 2014]. Figures A1c and A1d show two examples of this calculation, at times

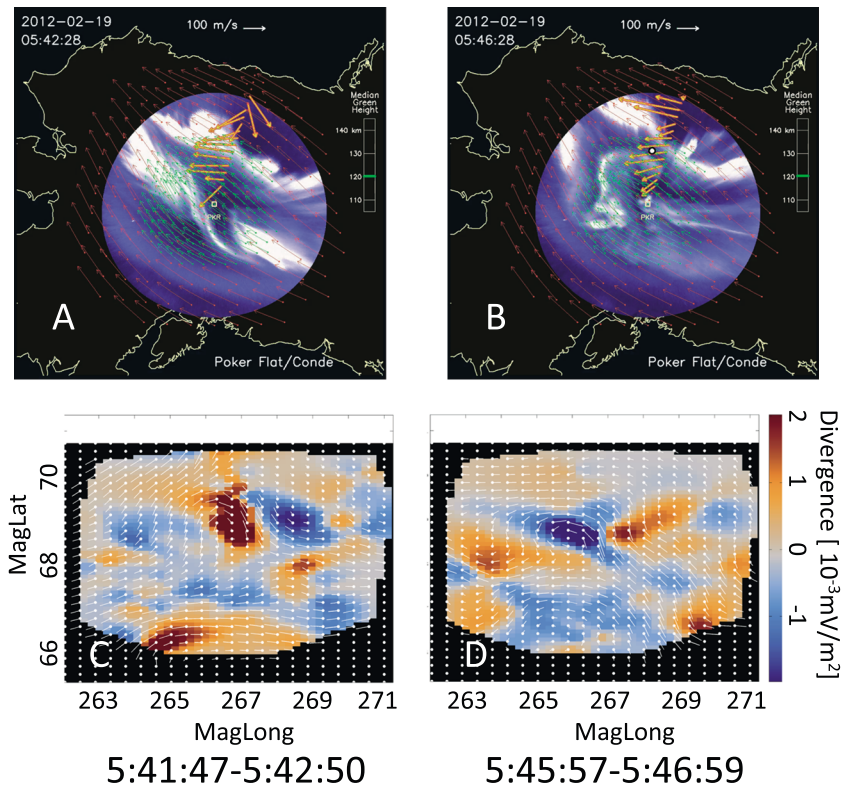


Figure A1. Two different representations of the electric field measured by PFISR. (a and b) (orange arrows) The plasma flow along the central axis of the PFISR beam field, using a 1-D calculation [Heinselmann and Nicolls, 2008], assuming only latitudinal variation. These panels also show neutral wind vectors from SDI and an underlying all-sky image for context, in a geographical coordinate system. (c and d) (red and blue colors) The divergence of \mathbf{E} after fitting for a 2-D electric field, with blue signifying consistency with an upward FAC, as per equation (1). The white markers indicate the 2-D-fitted plasma flow assimilated from the PFISR data. Figures A1c and A1d are in geomagnetic coordinates covering only the PFISR field of view.

matching Figures A1a and A1b, from before (left) and during (right) the MICA rocket flight. Note that these lower diagrams are oriented along magnetic latitude and longitude, while the upper are in geographic; the line of origins of the orange 1-D PFISR flow arrows trace out the center of the PFISR beam field, which is aligned along geomagnetic north. The “PKR” marker indicating Poker Flat Research Range is at 65.6° magnetic latitude; note that this center point of the upper imagery is the bottom boundary of the lower panels, which are limited to the PFISR field of view.

Figures A1a and A1c compare these large-scale electric field signatures near the passage of the preflight westward traveling surge. A strong region of precipitation (divergence in blue, upward field-aligned current (FAC) as per equation (1) is evident in the northeast region of the PFISR field, consistent with a knot of precipitation moving toward PFISR in the upper image just to the right of the PFISR centerline. The right column looks at signatures during the latter portion of the flight while the payload is exiting arcB (the time interval of the PFISR analysis corresponds to flight times T+290–T+352s.) The lower portion of Figure A1d shows blue signatures consistent with the various pieces and remnants of arcA and arcB. The red tongue on the left side of Figure A1d at magnetic latitudes near 68° corresponds to the region of downward current being traversed by the payload (note the payload marker along the trajectory in Figure A1b). The divergence of \mathbf{E} calculated by this PFISR 2-D analysis in these two regions is of the order $1\text{E}-6\text{ V/m}^2$ (positive for downward current regions, negative for upward); later, we will compare these values to the divergence of \mathbf{E} observed by the payload and to that calculated by an ionospheric model. We note, in comparing the top and bottom panels of Figure A1, that the 1-D solutions (Figures A1a and A1b, orange arrows) assume longitudinal invariance in the flows, whereas the 2-D solutions (Figures A1c and A1d, white arrow flow field) show structured flows at this time.

Since the PFISR electric fields are computed from plasma $\mathbf{E} \times \mathbf{B}$ drifts, the corresponding $\nabla \cdot \mathbf{E}$ calculations do not fully quantify impacts of neutral winds on field-aligned currents. Other terms are needed to compute neutral wind influence on FACs, (cf. equations (4) and (5) which are used in section 5 for this purpose).

Acknowledgments

The MICA analysis is dedicated to the memory of Paul M Kintner, Jr. MICA analysis work at Dartmouth College was funded by NASA grant NNX10AL18G and by Dartmouth College's Presidential Scholar and Senior Honors Thesis programs. Work at ERAU was funded by NSF Career award AGS-1255181, at UAF/GI by NASA grant NNX10AL20G, and at Cornell by NASA grant NNX10AL16G. Work at UIO has been supported by the ESA PRODEX contract 4200090335 and the Research Council of Norway grant 208006. The MICA team thanks the engineering group at NASA Wallops and NSROC for their hard work and dedication to sounding rocket missions. The MICA project was aided by SRI/PFISR and by the UAF/GI staff at Poker Flat Research Range. The authors thank both reviewers for constructive and thoughtful reviews and wish to acknowledge useful conversations about the ionospheric Alfvén resonator (IAR) with Robert Lysak. Data may be requested from the lead author.

References

- Anderson, B. J., H. Korth, C. L. Waters, D. L. Green, and P. Stauning (2008), Statistical Birkeland current distributions from magnetic field observations by the iridium constellation, *Ann. Geophys.*, *26*(3), 671–687, doi:10.5194/angeo-26-671-2008.
- Anderson, C., M. Conde, and M. G. McHarg (2012a), Neutral thermospheric dynamics observed with two scanning Doppler imagers: 1. Monostatic and bistatic winds, *J. Geophys. Res.*, *117*, A03304, doi:10.1029/2011JA017041.
- Anderson, C., M. Conde, and M. G. McHarg (2012b), Neutral thermospheric dynamics observed with two scanning Doppler imagers: 3. horizontal wind gradients, *J. Geophys. Res.*, *117*, A05311, doi:10.1029/2011JA017471.
- Bekkeng, T. A., K. S. Jacobsen, J. K. Bekkeng, A. Pedersen, T. Lindem, J. Lebreton, and J. I. Moen (2010), Design of a multi-needle Langmuir probe system, *Meas. Sci. Technol.*, *21*, 85903, doi:10.1088/0957-0233/21/8/085903.
- Blelly, P., C. Lathuilière, B. Emery, J. Liliensten, J. Fontanari, and D. Alcaydé (2005), An extended TRANSCAR model including ionospheric convection: Simulation of EISCAT observations using inputs from AMIE, *Ann. Geophys.*, *23*, 419–431.
- Brekke, A. (1997), *Physics of the Upper Polar Atmosphere*, Wiley-Praxis Series in Atmospheric Physics, Wiley, Chichester, U. K.
- Chaston, C. C., J. W. Bonnell, C. W. Carlson, M. Berthomier, L. M. Peticolas, I. Roth, J. P. McFadden, R. E. Ergun, and R. J. Strangeway (2002), Electron acceleration in the ionospheric Alfvén resonator, *J. Geophys. Res.*, *107*(A11), 1413, doi:10.1029/2002JA009272.
- Clausen, L. B. N., J. B. H. Baker, J. M. Ruohoniemi, S. E. Milan, and B. J. Anderson (2012), Dynamics of the region 1 Birkeland current oval derived from the active magnetosphere and planetary electrodynamics response experiment (ampere), *J. Geophys. Res.*, *117*, A06233, doi:10.1029/2012JA017666.
- Cohen, I. J., et al. (2013), Auroral current and electrodynamics structure (ACES) observations of ionospheric feedback in the Alfvén resonator and model responses, *J. Geophys. Res. Space Physics*, *118*(6), 3288–3296, doi:10.1002/jgra.50348.
- Conde, M., and R. W. Smith (1998), Spatial structure in the thermospheric horizontal wind above Poker Flat, Alaska, during solar minimum, *J. Geophys. Res.*, *103*, 9449–9471, doi:10.1029/97JA03331.
- Dahlgren, H., G. W. Perry, J. L. Semeter, J.-P. St.-Maurice, K. Hosokawa, M. J. Nicolls, M. Greffen, K. Shiokawa, and C. Heinselman (2012), Space-time variability of polar cap patches: Direct evidence for internal plasma structuring, *J. Geophys. Res.*, *117*, A09312, doi:10.1029/2012JA017961.
- Dahlgren, H., B. S. Lanchester, and N. Ivchenko (2015), Coexisting structures from high- and low-energy precipitation in fine-scale aurora, *Geophys. Res. Lett.*, *42*, 1290–1296, doi:10.1002/2015GL063173.
- de Boer, J. D., J. A. Noel, and J. St.-Maurice (2010), The effects of mesoscale regions of precipitation on the ionospheric dynamics, electrodynamic and electron density in the presence of strong ambient electric fields, *Ann. Geophys.*, *28*, 1345–1360, doi:10.5194/angeo-28-1345-2010.
- Doe, R. A., M. Mendillo, J. Vickrey, L. Zanetti, and R. Eastes (1993), Observations of nightside auroral cavities, *J. Geophys. Res.*, *98*, 293–310.
- Frederick-Frost, K. M., K. A. Lynch, P. M. Kintner, E. Klatt, D. Lorentzen, J. Moen, Y. Ogawa, and M. Widholm (2007), SERSIO: Svalbard EISCAT rocket study of ion outflows, *J. Geophys. Res.*, *112*, A08307, doi:10.1029/2006JA011942.
- Heinselman, C. J., and M. J. Nicolls (2008), A Bayesian approach to electric field and E-region neutral wind estimation with the Poker Flat Advanced Modular Incoherent Scatter Radar, *Radio Sci.*, *43*, R5013, doi:10.1029/2007RS003805.
- Horak, P. (2014), Attitude estimation for rocket-borne sensorcraft, Senior Honors Thesis, Dep. of Phys. and Astron., Dartmouth College, Hanover, N. H.
- Huba, J. D., G. Joyce, and J. A. Fedder (2000), Sami2 is another model of the ionosphere (SAMI2): A new low-latitude ionosphere model, *J. Geophys. Res.*, *105*, 23,035–23,054, doi:10.1029/2000JA000035.
- Hwang, K.-J., K. A. Lynch, C. W. Carlson, J. W. Bonnell, and W. J. Peria (2006a), Fast auroral snapshot observations of perpendicular DC electric field structures in downward auroral current regions: Morphology, *J. Geophys. Res.*, *111*, A09205, doi:10.1029/2005JA011471.
- Hwang, K.-J., K. A. Lynch, C. W. Carlson, J. W. Bonnell, and W. J. Peria (2006b), Fast auroral snapshot observations of perpendicular DC electric field structures in downward current regions: Implications, *J. Geophys. Res.*, *111*, A09206, doi:10.1029/2005JA011472.
- Hysell, D., R. Miceli, J. Munk, D. Hampton, C. Heinselman, M. Nicolls, S. Powell, K. Lynch, and M. Lessard (2012), Comparing VHF coherent scatter from the radar aurora with incoherent scatter and all-sky auroral imagery, *J. Geophys. Res.*, *117*(A10), doi:10.1029/2012JA018010.
- Jacobsen, K. S., A. Pedersen, J. I. Moen, and T. A. Bekkeng (2010), A new Langmuir probe concept for rapid sampling of space plasma electron density, *Meas. Sci. Technol.*, *21*(8), 85902, doi:10.1088/0957-0233/21/8/085902.
- Kaeppler, S. R. (2013), A rocket-borne investigation of auroral electrodynamics within the auroral ionosphere, PhD thesis, Univ. of Iowa, Iowa City.
- Karlsson, T., N. Brenning, O. Marghitu, G. Marklund, and S. Buchert (2007), High-altitude signatures of ionospheric density depletions caused by field-aligned currents, *Space Phys.*, arXiv:0704.1610v1 [physics.space-ph].
- Kelley, M. C. (1989), *The Earth's Ionosphere*, Academic Press, San Diego, Calif.
- Knudsen, D. J., M. C. Kelley, G. D. Earle, J. P. Vickrey, and M. H. Boehm (1990), Distinguishing Alfvén waves from quasi-static field structures associated with the discrete aurora: Sounding rocket and HILAT satellite measurements, *Geophys. Res. Lett.*, *17*, 921–924.
- Lanchester, B. S., K. Kaila, and I. W. McCrea (1996), Relationship between large horizontal electric fields and auroral arc elements, *J. Geophys. Res.*, *101*(A3), 5075–5084, doi:10.1029/95JA02055.
- Lanchester, B. S., M. H. Rees, K. J. F. Sedgemore, J. R. Palmer, H. U. Frey, and K. U. Kaila (1998), Ionospheric response to variable electric fields in small-scale auroral structures, *Ann. Geophys.*, *16*(10), 1343–1354, doi:10.1007/s00585-998-1343-8.
- Liliensten, J., and P. Blelly (2002), The TEC and F2 parameters as tracers of the ionosphere and thermosphere, *J. Atmos. Sol. Terr. Phys.*, *64*, 775–793.
- Lummerzheim, D., and J. Liliensten (1994), Electron transport and energy degradation in the ionosphere: Evaluation of the numerical solution, comparison with laboratory experiments and auroral observations, *Ann. Geophys.*, *12*, 1039–1051, doi:10.1007/s00585-994-1039-7.
- Lundberg, E. T., P. M. Kintner, K. A. Lynch, and M. R. Mella (2012a), Multi-payload measurement of transverse velocity shears in the topside ionosphere, *Geophys. Res. Lett.*, *39*, L01107, doi:10.1029/2011GL050018.
- Lundberg, E. T., P. M. Kintner, S. P. Powell, and K. A. Lynch (2012b), Multipayload interferometric wave vector determination of auroral hiss, *J. Geophys. Res.*, *117*, A02306, doi:10.1029/2011JA017037.
- Lynch, K. A., J. L. Semeter, M. Zettergren, P. Kintner, R. Arnoldy, E. Klatt, J. LaBelle, R. Michell, E. MacDonald, and M. Samara (2007), Auroral ion outflow: Low altitude energization, *Annales Geophys.*, *25*, 1967–1977.

- Lysak, R. L. (1985), Auroral electrodynamics with current and voltage generators, *J. Geophys. Res.*, *90*, 4178–4190.
- Lysak, R. L. (1991), Feedback instability of the ionospheric resonant cavity, *J. Geophys. Res.*, *96*, 1553–1568.
- Lysak, R. L. (1999), Propagation of Alfvén waves through the ionosphere: Dependence on ionospheric parameters, *J. Geophys. Res.*, *104*, 10,017–10,030, doi:10.1029/1999JA900024.
- Lysak, R. L., and Y. Song (2011), Development of parallel electric fields at the plasma sheet boundary layer, *J. Geophys. Res.*, *116*, A00K14, doi:10.1029/2010JA016424.
- Mallinckrodt, A. J., and C. W. Carlson (1978), Relations between transverse electric fields and field aligned currents, *J. Geophys. Res.*, *83*, 1426–1432.
- Marklund, G. T., et al. (2001), Temporal evolution of acceleration structures in the auroral return current region, *Nature*, *414*, 724–727.
- Michell, R. G., K. A. Lynch, and H. C. Stenbaek-Nielsen (2008), Ground-based observational signature of a downward current channel in an active auroral arc, *Geophys. Res. Lett.*, *35*, L08101, doi:10.1029/2008GL033596.
- Moen, J., K. Oksavik, T. Abe, M. Lester, Y. Saito, T. A. Bekkeng, and K. S. Jacobsen (2012), First in-situ measurements of HF radar echoing targets, *Geophys. Res. Lett.*, *39*, L07104, doi:10.1029/2012GL051407.
- Moore, T. E., and J. L. Horwitz (2007), Stellar ablation of planetary atmospheres, *Rev. Geophys.*, *45*(3), RG3002, doi:10.1029/2005RG000194.
- Newell, P. T., T. Sotirelis, and S. Wing (2009), Diffuse, monoenergetic, and broadband aurora: The global precipitation budget, *J. Geophys. Res.*, *114*, A09207, doi:10.1029/2009JA014326.
- Nicolls, M. J., R. Cosgrove, and H. Bahcivan (2014), Estimating the vector electric field using monostatic, multi-beam incoherent scatter radar measurements, *Radio Sci.*, *1124*–1139, doi:10.1002/2014RS005519.
- Noël, J., J. St.-Maurice, and P. Blelly (2000), Nonlinear model of short-scale electrodynamics in the auroral ionosphere, *Ann. Geophys.*, *18*, 1128–1144, doi:10.1007/s005850000265.
- Noël, J.-M. A., J.-P. St.-Maurice, and P.-L. Blelly (2005), The effect of E-region wave heating on electrodynamical structures, *Ann. Geophys.*, *23*, 2081–2094, doi:10.5194/angeo-23-2081-2005.
- Paschmann, G. (2002), Auroral plasma physics, *Space Sci. Rev.*, *103*, 1–475.
- Rees, M. H., and D. Luckey (1974), Auroral electron energy derived from ration of spectroscopic emissions 1. Model computations, *J. Geophys. Res.*, *79*, 5181–5186.
- Reiff, P. H. (1984), Models of auroral-zone conductances, in *Magnetospheric Currents*, *Geophys. Monogr. Ser.*, vol. 28, edited by T. A. Potemra, pp. 180, AGU, Washington, D. C.
- Russell, A. J. B., A. N. Wright, and A. W. Hood (2010), Self-consistent ionospheric plasma density modifications by field-aligned currents: Steady state solutions, *J. Geophys. Res.*, *115*, A04216, doi:10.1029/2009JA014836.
- Russell, A. J. B., A. N. Wright, and A. V. Streltsov (2013), Production of small-scale Alfvén waves by ionospheric depletion, nonlinear magnetosphere-ionosphere coupling and phase mixing, *J. Geophys. Res. Space Physics*, *118*, 1450–1460, doi:10.1002/jgra.50168.
- Semeter, J., and R. Doe (2002), On the proper interpretation of ionospheric conductance estimated through satellite photometry, *J. Geophys. Res.*, *107*(A8), 1200, doi:10.1029/2001JA009101.
- Semeter, J., T. Butler, C. Heinselman, M. Nicolls, J. Kelly, and D. Hampton (2009), Volumetric imaging of the auroral ionosphere: Initial results from PFISR, *J. Atmos. Sol. Terr. Phys.*, *71*, 738–743, doi:10.1016/j.jastp.2008.08.014.
- Solomon, S. C., and L. Qian (2005), Solar extreme-ultraviolet irradiance for general circulation models, *J. Geophys. Res.*, *110*, A10306, doi:10.1029/2005JA011160.
- St.-Maurice, J., W. Kofman, and D. James (1996), In situ generation of intense parallel electric fields in the lower ionosphere, *J. Geophys. Res.*, *101*, 335–356, doi:10.1029/95JA02586.
- Streltsov, A. V., and W. Lotko (2008), Coupling between density structures, electromagnetic waves and ionospheric feedback in the auroral zone, *J. Geophys. Res.*, *113*, A05212, doi:10.1029/2007JA012594.
- Strickland, D. J., R. R. Meier, J. H. Hecht, and A. B. Christensen (1989), Deducing composition and incident electron spectra from ground-based auroral optical measurements: Theory and model results, *J. Geophys. Res.*, *94*, 13,527–13,539.
- Zettergren, M., and J. Semeter (2012), Ionospheric plasma transport and loss in auroral downward current regions, *J. Geophys. Res.*, *117*, A06306, doi:10.1029/2012JA017637.
- Zettergren, M., and J. Snively (2013), Ionospheric signatures of acoustic waves generated by transient tropospheric forcing, *Geophys. Res. Lett.*, *40*, 5345–5349, doi:10.1002/2013GL058018.
- Zettergren, M., J. Semeter, B. Burnett, W. Oliver, C. Heinselman, P.-L. Blelly, and M. Diaz (2010), Dynamic variability in F-region ionospheric composition at auroral arc boundaries, *Ann. Geophys.*, *28*(2), 651–664, doi:10.5194/angeo-28-651-2010.
- Zettergren, M., K. Lynch, D. Hampton, M. Nicolls, B. Wright, M. Conde, J. Moen, M. Lessard, R. Miceli, and S. Powell (2014), Auroral ionospheric F region density cavity formation and evolution: MICA campaign results, *J. Geophys. Res. Space Physics*, *119*, 3162–3178, doi:10.1002/2013JA019583.